Temporal and spatial evolution of nuclear polarization in optically pumped InP

J. B. Miller,[1,*] C. A. Klug,[1] K. L. Sauer,[1,2] and J. P. Yesinowski[1]

[1]*Naval Research Laboratory, Code 6122, Washington, DC 20375-5342, USA*

[2]*Department of Physics and Astronomy, George Mason University, 4400 University Drive MS 3F3, Fairfax, Virginia 22030, USA*

(Received 30 October 2014; revised manuscript received 23 March 2015; published 8 June 2015)

The electron-nuclear interaction in optically pumped NMR of semiconductors manifests itself through changes in spectral features (resonance shifts, linewidths, signal amplitudes) and through the magnitude of the nuclear-spin polarization. We show that these spectral features can provide a measure of the parameters that govern the optical pumping process: electron-nuclear cross-relaxation rate, Bohr radius and fractional occupancy of the optically relevant defect (ORD), and electron polarization at the ORD. Applying a model of the spatial and temporal evolution of the nuclear spins under optical pumping to ^{31}P in semi-insulating InP we find an ORD Bohr radius of 6 nm, independent of the electron polarization used to fit the data, confirming the ORD is a shallow donor. For an electron polarization of -0.15, the ORD fractional occupancy is 0.02, leading to an electron-nuclear cross-relaxation time of 0.20 s and a hyperfine frequency shift of 8.1 kHz for super-bandgap irradiation. Allowing the electron polarization to vary in the model constrained to the hyperfine shift data, we find the fractional occupancy and electron-nuclear cross-relaxation rate to be approximately inversely proportional to the electron polarization. From the long-time evolution of the nuclear polarization we calculate an ORD density of 5×10^{15} cm^{-3}.

DOI: 10.1103/PhysRevB.91.245205 PACS number(s): 76.60.Jx, 33.80.Be, 78.30.Fs

I. INTRODUCTION

The generation of high nuclear-spin polarizations within bulk semiconductors such as Si, GaAs, and InP by means of optical irradiation near the band gap at low temperatures (optical pumping) is a topic of long-standing interest [1]. Achieving a detailed understanding of the fundamental physical processes leading to such high polarizations has proven very challenging, but considerable progress has been made in recent decades. In particular, the direct detection of the enhanced nuclear polarization by conventional nuclear magnetic resonance techniques (optically pumped NMR, or OPNMR) has provided valuable new insights [2–4]. The basic process involved in all cases is a dynamic nuclear polarization of the nuclear-spin system by photoexcited electron spins having a nonequilibrium spin polarization. In experiments involving unpolarized or linearly polarized light the electron spin system is saturated, resulting in an optical Overhauser enhancement. Much greater deviations from the thermal equilibrium electron-spin polarization can be achieved by employing circularly polarized light, whose differing transition probabilities between magnetic subbands of both valence band and conduction band can result in large electron-spin polarizations, and consequently much higher nuclear polarizations. We present ^{31}P OPNMR results for this latter type of experiment, in a semi-insulating InP sample doped with Fe^{3+} as acceptors to compensate for the typically n-type nature of InP due to P vacancies.

After GaAs, InP has been the semiconductor most extensively investigated by OPNMR, with NMR detected from both ^{31}P [5–7] and ^{115}In [8–10]. The 100% naturally abundant spin-1/2 nucleus ^{31}P in InP has been proposed as a favorable nucleus for "transferred OPNMR," or TOPNMR, in which the hyperpolarization of the surface nuclei of a semiconductor could in principle be transferred to other nuclei in an adsorbed layer by means of cross-polarization or cross-relaxation processes [11]. Although cross polarization across such an InP interface has been demonstrated without optical pumping [12], TOPNMR will require knowledge of and control over factors influencing both electron- and nuclear-spin polarization in the semiconductor surface layers at the atomic level.

The photoexcited spin-polarized electrons created by optical pumping are generally believed to transfer their hyperpolarization by cross relaxation to nuclear spins via localized sites that have, in lieu of precise structural characterization, been termed "optically relevant defects" (ORDs). The holes associated with these photoelectrons are generally neglected because their spin orientation is quickly destroyed through spin-orbit coupling in unstrained crystals of the GaAs or InP type [1]. The delocalized electrons in the conduction band have been shown by optically detected NMR (ODNMR) in GaAs to undergo spin exchange with localized electrons at the ORDs, resulting in an efficiently averaged electronic spin state [13]. Evidence for the existence of localized electrons at ORD sites comes from the small electron-nucleus hyperfine shifts observed with the light on in OPNMR of both GaAs and InP [7,14–16]. The ORD sites with trapped electrons in the presence of light have generally been assumed to act as shallow donors, with the unpaired electron in a hydrogenic s orbital having a Bohr radius a_0 of many nanometers. The fractional number of ORD sites having trapped electrons depends on the intensity of irradiation.

Through the Fermi contact mechanism nuclei that are far from the center of the ORD compared to a_0 experience a hyperfine interaction responsible for the cross relaxation that polarizes the nuclear spins. We have previously shown [7] in semi-insulating InP that this contact mechanism, rather than a direct electron-nucleus dipolar mechanism [8,10], or coupling of nuclei to conduction electrons, is consistent with the experimental results. In this paper we will present additional

*Author to whom correspondence should be addressed: joel.miller@nrl.navy.mil

evidence of this mechanism. At long pumping times the ^{31}P magnetization is transported from the region of the ORD by spin diffusion. Spin diffusion aids cross relaxation near the ORD by redistributing polarization to more distant regions.

In order to assess the influence of photon energy on the average nuclear polarization generated by OPNMR, it is insufficient to consider merely the total NMR signal intensity. This is so because light at lower energies (e.g., sub-bandgap) penetrates a bulk sample to greater depths; in such cases the interplay between the (generally reduced) degree of local polarization and the increased number of nuclei affected due to the greater penetration depth determines the resultant overall OPNMR signal intensity. These two competing effects of local polarization and penetration depth were sorted out by using stray-field NMR imaging (STRAFI) to measure the ^{31}P OPNMR signal in InP with micron spatial resolution as a function of depth from the surface [5]. These results, as well as our own results [7], showed that super-bandgap photons are more efficient at generating high local nuclear polarizations than sub-bandgap photons.

In this paper, we compare experimental results with theoretical modeling to better understand the temporal and spatial evolution of ^{31}P nuclear-spin polarization in OPNMR experiments on semi-insulating InP as a result of the combined effects of cross relaxation, spin diffusion, and spin-lattice relaxation. "Temporal" refers to the buildup of OPNMR signal intensity and polarization as a function of irradiation time, with varying photon energy, light intensity, and temperature. "Spatial" refers to two distinct spatial scales, the microscopic one around the ORD and the macroscopic one involving penetration depth. Applying the theoretical model to the spatiotemporal results at short pumping times, less than approximately 64 s, provides a value for the ORD Bohr radius and fractional occupancy which, in turn, allows the calculation of the cross-relaxation rate and nuclear hyperfine shift. Results at longer pumping times place a lower limit on the electron polarization and give information about both the propagation of nuclear polarization from the ORDs via spin diffusion and the number density of ORDs.

II. THEORETICAL BACKGROUND

The model for the temporal and spatial development of nuclear polarization in optically pumped semiconductors has been described in detail elsewhere [13,14,17,18]. Here we discuss the features of the model pertinent to our results. Previous work focused on temporal evolution through growth of the signal amplitude and nuclear polarization. In the present study we add to this the use of light-induced nuclear resonance shifts to monitor spatial evolution.

In optically pumped semiconductors, nuclear polarization is created via cross relaxation with a polarized electron. The nuclear polarization extends into the sample through a combination of direct polarization by the polarized electron and nuclear-spin diffusion. In order to describe how the nuclear polarization evolves both in time and space under constant irradiation, we define a normalized nuclear differential polarization,

$$\mathcal{M}(r,\tau_L) = \frac{I_z(r,\tau_L) - I_{eq}}{I_\infty - I_{eq}}, \tag{1}$$

where r is the distance between the nucleus and the nearest ORD, τ_L is the irradiation time, and I_{eq} is the thermal equilibrium value of the average nuclear spin. The limiting average nuclear spin I_∞ is given by [1,19]

$$I_\infty = \frac{J_z - J_{eq}}{1 - 4J_z J_{eq}}, \tag{2}$$

where J_{eq} is the thermal equilibrium average electron spin. Using the InP conduction electron g factor [20,21] we obtain $J_{eq} = -0.08$ at 2.35 T and 6 K. The average electron spin J_z is given by [19]

$$J_z = \frac{J_0 + J_{eq}\tau/\tau_s}{1 + \tau/\tau_s}, \tag{3}$$

where τ is the electron lifetime in the conduction band, τ_s is the electron-spin lifetime, and J_0 is the initial average electron spin from optical pumping. An upper limit is placed on J_z by J_0, usually taken to be ± 0.25 depending on light helicity [22], although recent calculations suggest that significant deviation from this value is possible [23]. With knowledge of I_∞ a lower limit can be placed on J_z through Eq. (2).

The model we use is based on the premise that optical pumping creates spin-polarized photoelectrons, some of which become trapped at ORDs, and includes these simplifying assumptions about the ORDs:

(1) the ORDs are unoccupied when the light is off;

(2) the ORDs are uniformly distributed throughout the material and are surrounded by a sphere of influence within which only one ORD is responsible for polarizing the nuclei, either directly or through spin diffusion;

(3) spheres of influence are of uniform size with radius $r_{\max}$, and touch at the edges, resulting in the ORD number density of $(2r_{\max})^{-3}$;

(4) interactions within the spheres of influence are isotropic.

These assumptions lead to the boundary condition that there is no spin diffusion across $r_{\max}$, i.e., nuclear polarization does not leak out of the sphere of influence.

So far, we have described ORDs that are identical. In reality we expect polarization to build up around ORDs differently, depending on the distance of the ORD from the surface. The drop in light intensity with distance d from the surface will alter the local photoexcited electron density. If $r_{\max}$ is much smaller than the characteristic distance for light falloff from the surface, the two distances can be treated separately. Therefore, the normalized nuclear differential polarization depends on three parameters, r, d, and τ_L. In subsequent discussion we use $\mathcal{M}$ to denote $\mathcal{M}(r,d,\tau_L)$ or the dependence of $\mathcal{M}$ on any of the reduced forms of these parameters introduced later.

The time evolution of $\mathcal{M}$ can be written as a sum of terms due to diffusion, electron cross relaxation, and nuclear-spin-lattice relaxation in analogy with the equation for nuclear-spin relaxation due to paramagnetic impurities originally written by Bloembergen [24]:

$$\frac{\partial \mathcal{M}}{\partial \tau_L} = D\nabla^2\mathcal{M} + \frac{1}{T_{1C}(r,d^\dagger)}[1 - \mathcal{M}] - \frac{\mathcal{M}}{T_{1L}(d^\dagger)}, \tag{4}$$

where D is the nuclear-spin-diffusion constant, $1/T_{1C}(r,d^\dagger)$ is the electron-nuclear cross-relaxation rate, and $1/T_{1L}(d^\dagger)$ is the spin-lattice relaxation rate due to all other mechanisms, where the subscript "L" refers to the light being on, thus possibly

providing additional relaxation pathways to the lattice [22]. Any dependence of these relaxation times on the normalized distance, $d^\dagger = d/d_0$, from the surface, will be determined by the relaxation mechanism, as discussed below. The variable d_0 is the optical absorption depth and is photon energy dependent. For definiteness we will assume the electron is in a $1s$ hydrogenic orbital around the ORD, with a Bohr radius of a_0, and that cross relaxation proceeds through the contact hyperfine interaction. The hyperfine interaction contains both a contact term and a through-space, or dipolar, term [25]. Bagraev and Vlasenko [26] showed that the dominant hyperfine term at a distance from the ORD where the spin-diffusion rate equals the cross-relaxation rate corresponds to the interaction that dominates polarization of the spins. We will show that, for InP, spin diffusion should dominate at distances greater than 2 nm from the center of the ORD, which is less than the Bohr radius if the ORDs are comprised of shallow donors; calculations of the relative size of the hyperfine terms at this distance suggest the contact mechanism is expected to be the dominant hyperfine term [27]. Then at a distance r from the closest ORD, and a distance $d^\dagger$ from the surface, the cross-relaxation rate is $1/T_{1C}(r,d^\dagger) = e^{-4r/a_0}/T_{1C}(0,d^\dagger)$ with an associated hyperfine frequency shift of $f(r,d^\dagger) = f_0(d^\dagger)e^{-2r/a_0}$.

From Eq. (4) we see that in order to have high macroscopic nuclear polarization we need the electron polarization to be high and for

$$\frac{1}{T_{1C}(0,d^\dagger)}, \frac{D^*}{r^{*2}_{\max}} \gg \frac{1}{T_{1L}(d^\dagger)}, \tag{5}$$

where $*$ indicates we have scaled the distance by a_0 such that $D^* = D/a_0^2$ and $r^* = r/a_0$. This highlights the competition between localized buildup of polarization, $1/T_{1C}(0,d^\dagger)$, diffusion of polarization, $D^*/r^{*2}_{\max}$, and loss of polarization through spin-lattice relaxation, $1/T_{1L}(d^\dagger)$. From this one can see there are many possible combinations of constants that would yield a high nuclear polarization. The spin-diffusion coefficient for the particular crystal orientation used, D, and Bohr radius a_0 are properties of the material, but the latter might vary across different types of ORDs, while sub- and super-bandgap irradiation might populate different sites depending on their energy levels. Different types of ORDs would also have different spacing from one another, i.e., lead to variations in $r_{\max}$. The two time constants, T_{1C} and T_{1L} will depend both on the intensity of light and the magnetic-field strength. In general one wants to obtain high nuclear polarization rapidly, so choosing conditions which maximize the buildup rate, yet under the constraints of Eq. (5), is desirable.

For short pumping times, we can neglect the spin-lattice relaxation, and Eq. (4) can be simplified to

$$\frac{\partial \mathcal{M}}{\partial \tau_L} = D^* \nabla^{*2} \mathcal{M} + \frac{f^2}{f_0^2(d^\dagger) T_{1C}(0,d^\dagger)}[1 - \mathcal{M}]. \tag{6}$$

Furthermore, we can treat the exterior boundary condition at $r^*_{\max}$ as being very far away compared to the length scales of interest at these short pumping times. Using the ^{31}P NMR spectra in which frequency shifts reflect the distance from the ORD to give spatial evolution and using experiments at different pumping times to give the temporal evolution, we analyze the simultaneous evolution of $\mathcal{M}$ and f to find D^* and the combined constant $f_0^2(d^\dagger)T_{1C}(0,d^\dagger)$. By calculating D [28], we can further obtain a_0. The combined constant $f_0^2(d^\dagger)T_{1C}(0,d^\dagger)$ is independent of a_0 since both $1/T_{1C}(0,d^\dagger)$ and $f_0^2(d^\dagger)$ are proportional to the square of the electron density [1,13], but is proportional to FJ_z^2 where F is the fractional occupancy of the ORD.

After a few minutes of pumping the light-induced frequency shifts disappear. At longer pump times a small, but significant, frequency shift due to the nuclear magnetization emerges and grows. The measurement of these shifts gives us the average nuclear polarization [7]. Measuring the net signal and absolute polarization, coupled with the constants determined from short pumping time behavior, permits constraints on the possible values for J_z (and therefore F), $r_{\max}$, and T_{1L}.

A. Nuclear relaxation mechanisms

Turning now to relaxation mechanisms for cross relaxation between nuclei and the electron at the ORD, the contact hyperfine interaction [29] with an r dependence based on a hydrogenic $1s$ orbital is given by [13]

$$\frac{1}{T_{1C}(r^*,d^\dagger)} = \left[\left(\frac{A_0}{2\hbar}\frac{v_0}{\pi}\right)^2 \frac{2\tau_c}{1+\omega_j^2\tau_c^2}\right] \frac{F(1-4J_zJ_{eq})}{a_0^6} e^{-4r^*}. \tag{7}$$

In the above equation ω_j is the precession frequency of the electron spin in the external field, τ_c is the correlation time of the electron at the ORD, i.e., the time constant of the hyperfine interaction fluctuation, and v_0 is the unit-cell volume. The fundamental hyperfine coupling constant A_0 is [30,31]

$$A_0 = \gamma_P \frac{8\pi}{3}\frac{\mu_0}{4\pi} g\mu_B \varrho \hbar, \tag{8}$$

where g is the g factor of the free electron and $\varrho = 3.26 \times 10^{31}/\mathrm{m}^3$ is the electron density at the phosphorus nuclei [30]. Using a hyperfine interaction fluctuation time constant of $\tau_c = 6$ ps [8], a value which is close to the optimal value of $\tau_c = 1/\omega_j$ for our field, we calculate the term in brackets in Eq. (7) to be 12×10^6 nm^6/s. Assuming negligible change in temperature with change in light intensity, the dominant variation in T_{1C} with $d^\dagger$ will appear through F. For a shallow donor, the predicted Bohr radius [32] is $\epsilon(m_e/m_e^*)(0.529\ \mathrm{nm}) = 7.7$ nm, where, at our experimental temperature of 6 K, the ratio of the effective mass of the electron in the conduction band m_e^* to that of the mass of the electron m_e is 8.05×10^{-2} and the dielectric constant ϵ is 11.8 [33].

At low temperature the most likely mechanism for nuclear-spin-lattice relaxation is through interaction with paramagnetic electron spins associated with impurities and defects:

$$\frac{1}{T_1} \propto \frac{1}{r_e^6}\frac{2\tau_s}{1+\omega_I^2\tau_s^2}, \tag{9}$$

where ω_I is the nuclear Larmor frequency [25]. The distance from the nucleus to the paramagnetic center is r_e. The nuclear T_1 of Fe-doped InP is 41 000 s at 8 K and 9.4 T [5]. We previously measured it to be 8760 s at 2.35 T and 5–6 K [7]. Using the ratio of the measured T_1's, and assuming the electron relaxation time to be field independent, we predict $\tau_s = 2.3$ ns,

in good agreement with the literature value of 2.7 ns for τ_s at high field and low temperature in InP [34], confirming the relaxation mechanism.

The mechanism of nuclear relaxation by paramagnetic electron spins is not inherently dependent on light intensity, however, D'yakonov and Perel' proposed that new paramagnetic centers can be created when optically excited conduction electrons are captured at deep traps [29]. This mechanism has the same field dependence as for the native paramagnetic centers discussed above. The relaxation rate from this mechanism will depend on the fractional occupancy of the trap sites in a manner similar to the cross-relaxation rate. We further assume that the positions of the paramagnetic centers are uncorrelated with the positions of the ORDs; therefore, averaging over all ORDs, the resultant spin-lattice relaxation time under illumination, T_{1L}, will be independent of r^*, varying only with $d^\dagger$.

B. Light intensity

We now consider the possible effects of light intensity on the nuclear relaxation rates and polarization buildup. We identify several general mechanisms by which light intensity may affect the buildup of nuclear polarization, in addition to simple heating. First, we consider the possibility that the electrons that are energetically allowed to undergo transitions to the conduction band, given the photon energy, are depleted under the highest intensities of irradiation. A calculation [35] of the density of such energetically favorable valence electrons for super-bandgap irradiation at 1.428 eV that can be excited from the top 4 meV of the valence band yields an estimate of 10^{17} valence electrons/cm^3. This is two orders of magnitude larger than the steady-state density of conduction electrons produced under typical optical pumping conditions, 10^{15} cm^{-3}, estimated for 1.428 eV light with an intensity of 3.4 W/cm^2, a photoelectron lifetime of 10 ns, and an absorption depth of 1 μm. Therefore, depletion of energetically favorable valence electrons can be ruled out.

Second, the light intensity may affect the electron lifetime and spin-relaxation time. The lifetime of photoelectrons in the conduction band has been observed to depend on the number of electrons in the conduction band, N_c, with the functional dependence varying with the recombination mechanism [36]. The interdependence of photoelectron lifetime and the concentration of conduction photoelectrons will affect the cross-relaxation rate not only through the ORD fractional occupancy, but also potentially through the dependence of J_z on τ [Eq. (3)]. Likewise, the photoelectron spin-relaxation time may also depend on N_c and therefore have an effect on J_z [Eq. (3)] [37].

Third, variations in light intensity will alter the local conduction electron density, which in turn can affect the fractional occupancy of the ORD's, thus altering $T_{1C}(r^*,d^\dagger)$. Fourth, variations in light intensity can affect the number of paramagnetic centers created, thus altering $T_{1L}(d^\dagger)$.

To arrive at a quantifiable understanding of the effects of light intensity on the time constants $T_{1C}(r^*,d^\dagger)$ and $T_{1L}(d^\dagger)$, we return to Eq. (4) and integrate over a single sphere of influence to find the net signal from that sphere:

$$\frac{d\int_\odot \mathcal{M}dV}{d\tau_L} = D\int_\odot \nabla^2\mathcal{M}dV + \int_\odot \frac{1}{T_{1C}(r^*,d^\dagger)}[1-\mathcal{M}]dV - \frac{1}{T_{1L}(d^\dagger)}\int_\odot \mathcal{M}dV. \quad (10)$$

We assume $\mathcal{M}$ is independent of $d^\dagger$ over the volume of integration, i.e., that $\mathcal{M}$ only depends on r^* in the volume of integration, which is reasonable if $r_{\max}$ is much smaller than d_0. Using the divergence, or Gauss's, theorem, in conjunction with the boundary condition $[\frac{\partial\mathcal{M}}{\partial r^*}]_{r^*=r^*_{\max}} = 0$ we find the diffusion term of Eq. (10) to be zero, and therefore when the system has reached the steady state,

$$\int_\odot \frac{1}{T_{1C}(r^*,d^\dagger)}dV = \int_\odot \mathcal{M}_\infty\left(\frac{1}{T_{1C}(r^*,d^\dagger)} + \frac{1}{T_{1L}(d^\dagger)}\right)dV, \quad (11)$$

where $\mathcal{M}_\infty \equiv \mathcal{M}(r^*,d^\dagger,\tau_L=\infty)$. Using Eq. (11) and the definition of $T_{1C}(r^*,d^\dagger) = T_{1C}(0,d^\dagger)e^{4r^*}$, we can rewrite Eq. (10) as

$$\frac{dm_\odot}{d\tau_L} = \frac{d\int_\odot \mathcal{M}dV}{d\tau_L} = \frac{1}{T_{1C}(0,d^\dagger)}\int_\odot [\mathcal{M}_\infty - \mathcal{M}]e^{-4r^*}dV + \frac{1}{T_{1L}(d^\dagger)}\int_\odot [\mathcal{M}_\infty - \mathcal{M}]dV, \quad (12)$$

where $m_\odot$ is the magnetization from a single sphere.

Following Lowe and Tse [38], the distribution of magnetization in the sphere is taken such that $m_\odot$ recovers exponentially with a time constant $T_B(d^\dagger)$,

$$m_\odot(\tau_L,d^\dagger) = m_\odot(\infty,d^\dagger)(1-e^{-\tau_L/T_B(d^\dagger)}). \quad (13)$$

We can then write the following:

$$\frac{dm_\odot}{d\tau_L} = \frac{d\int_\odot \mathcal{M}dV}{d\tau_L} = \frac{1}{T_B(d^\dagger)}\int_\odot (\mathcal{M}_\infty - \mathcal{M})dV. \quad (14)$$

Equating the right-hand side of Eqs. (12) and (14) finally gives

$$\frac{1}{T_B(d^\dagger)} = \frac{1}{T_{1L}(d^\dagger)} + \frac{1}{T_{1C}(0,d^\dagger)}\frac{\int_\odot(\mathcal{M}_\infty - \mathcal{M})e^{-4r^*}dV}{\int_\odot(\mathcal{M}_\infty - \mathcal{M})dV}. \quad (15)$$

This equation shows that $1/T_B(d^\dagger)$ is not extremely sensitive to the detailed shape of $\mathcal{M}$ [38].

Tycko introduced a phenomenological equation [11,14] relating light intensity to the nuclear signal intensity resulting from optical pumping:

$$m_\odot(\Phi,d^\dagger) = m^S_\odot\left(1-e^{-\Phi/\Phi_S e^{-d^\dagger}}\right), \quad (16)$$

where $m_\odot(\Phi,d^\dagger)$ emphasizes the dependence of $m_\odot$ on Φ and $d^\dagger$ in the limit of $\tau_L \ll T_B(d^\dagger)$. Here, Φ is the light intensity, Φ_S is the saturation light intensity, and $m^S_\odot$ is the saturation signal intensity. For optical pumping times $\tau_L \ll T_B(d^\dagger)$, Eq. (13) simplifies to

$$m_\odot(\tau_L,d^\dagger) = \frac{m_\odot(\infty,d^\dagger)\tau_L}{T_B(d^\dagger)}, \quad (17)$$

which then allows us to write

$$\frac{1}{T_B(d^\dagger)} \propto 1 - e^{-\Phi/\Phi_S e^{-d^\dagger}}. \tag{18}$$

From Eq. (15) we obtain the expressions

$$\frac{1}{T_{1C}(r^*,d^\dagger)} = \frac{1}{T_{1C}(0,0)} e^{-4r^*}\left(1 - e^{-\Phi/\Phi_S e^{-d^\dagger}}\right) \tag{19}$$

and

$$\frac{1}{T_{1L}(d^\dagger)} = \frac{1}{T_{1L}(0)}\left(1 - e^{-\Phi/\Phi_S e^{-d^\dagger}}\right). \tag{20}$$

C. Frequency shifts

At short pumping times, the polarized nuclei are relatively close to the ORD. Therefore, we study the spectra at early times to gain insight into the ORD and the growth of the signal at these early times. To elucidate the behavior of the spectra due to the presence of the polarized electron [7,14–16] we compare spectra in which the light is left on during data acquisition to spectra in which the light is turned off shortly before data acquisition.

The frequency shift experienced by a ^{31}P atom due to the hyperfine interaction with a 1s electron at position r^* is [1]

$$f(r^*) = \left[\frac{1}{2\pi}\frac{A_0}{2\hbar}\frac{v_0}{\pi}\right]\left(\frac{2J_z F}{a_0^3}\right) e^{-2r^*}. \tag{21}$$

We calculate the term in brackets to be 280 MHz nm^3. Comparing Eqs. (7) and (21) we see that the hyperfine shift and the cross-relaxation rate are well correlated [29]. Both quantities have a very strong dependence on a_0, to the negative third power for f and the positive sixth power for $T_{1C}(r^*,d^\dagger)$.

In addition to the isotropic frequency shift due to the hyperfine contact interaction, there would also be a shift due to the noncontact dipole interaction between the electron and nucleus. This shift, however, is anisotropic with an average of zero over a spherical volume around the electron; see the Appendix. Therefore, the net effect of the noncontact interaction would be to broaden the spectrum. As shown in the Appendix, for a 1s orbital, the broadening due to the noncontact interaction approaches that of the central shift due to the contact hyperfine interaction only when r^* is about 3 [27]; closer to the ORD the broadening would be less than the central shift.

The hydrogenic wave-function approximation, however, is only reasonable for shallow donors, such as those arising from substitutional donor atoms [32]. It has been shown that in addition to these shallow donors, there can be P_{In} antisites in InP with highly localized ("deep") wave functions [39,40]. From studies on Zn-doped InP, there is some indication that nuclear polarization builds up at P_{In} antisites [40]. In addition, it has been suggested that the Fe impurities in our sample could act as ORDs [5], and these would also be highly localized. Such high localization could significantly increase the broadening due to the noncontact dipolar interaction beyond that of the central shift due to the contact interaction, particularly at the shorter pumping times.

It has been suggested in fact that nuclear polarization builds up at multiple types of ORDs [34], so that one might expect to see a combination of purely hydrogenic wave functions, and those with a more localized distribution with a 1s tail outside the central cell. The short pumping times would be particularly sensitive to the exact nature of the electron distribution.

III. EXPERIMENTAL DETAILS

All experiments were performed at 2.35 T (40.5 MHz for ^{31}P) using a Tecmag console. The pulse sequences and data analysis methods were described previously [7]. A key aspect of all experiments was the saturation of both ^{31}P and ^{115}In nuclei before acquisition of the ^{31}P NMR signal. Whereas for most measurements a single light helicity σ_+^B was used along with spin echoes with pulse separations of 100 μs, for the determination of the ^{31}P polarization a string of small flip angle-free induction decays were acquired for σ_+^B and σ_-^B polarized light and the data were combined as described previously [7]. The photon energies were limited to two cases, sub-bandgap irradiation at 1.408 eV and super-bandgap irradiation at 1.428 eV [41]; these are represented by the subscripts sub and super respectively.

The semiconductor used in this work was a fragment of 348-μm-thick (100) orientation Fe-doped semi-insulating InP (Showa Denko lot 60706, carrier concentration 5.8–6.3 $\times$ 10^7 cm^{-3}, mobility 2500–2600 cm^2/V s, resistivity 3.3–3.6 $\times$ 10^{-3} Ω cm) [5], prepared as described previously [7].

The sample was maintained at 6 K in a Janis gas flow cryostat containing a home-built double resonance NMR probe. A Spectra Physics model 3900S Ti:sapphire laser with typical intensity at the cryostat window of 3.4 W/cm^2 was used for all experiments.

Equation (4), with Eqs. (19) and (20), was solved numerically in MATLAB using the built-in function *pdepe* with spherical symmetry. For the number of nuclei at a distance r^* from the ORD, a simple r^{*2} dependence was assumed. The solutions for 25 values of $d^\dagger$ ranging 0–5 were averaged to obtain the final fractional nuclear polarization as a function of r^*. First and second moments of the spectral line shapes were calculated from Eq. (21) weighted with the signal intensities from Eq. (4).

IV. RESULTS

A. Temperature dependence

The temperature dependence of signal and polarization buildup is important because of potential interest in optical pumping at higher temperatures, and because of the effects of laser heating of the sample. In particular, to quantify light intensity effects on the OPNMR signal, we must separate out the temperature effects of laser heating.

To probe these effects the temperature dependencies of the signal amplitude for irradiation with σ_+^B light and the nuclear polarization difference between irradiation with σ_+^B and σ_-^B light were measured with a laser power of 3.4 W/cm^2 and 800-s irradiation time (Fig. 1). We observe that the signal amplitude decreases linearly with increasing temperature. There is more scatter in the polarization data, but it too decreases with increasing temperature. For σ_+^B irradiation the signal decreases by 1.8%/K with the fit normalized to the extrapolated signal amplitude at 0 K, and the polarization decreases by 0.7%/K.

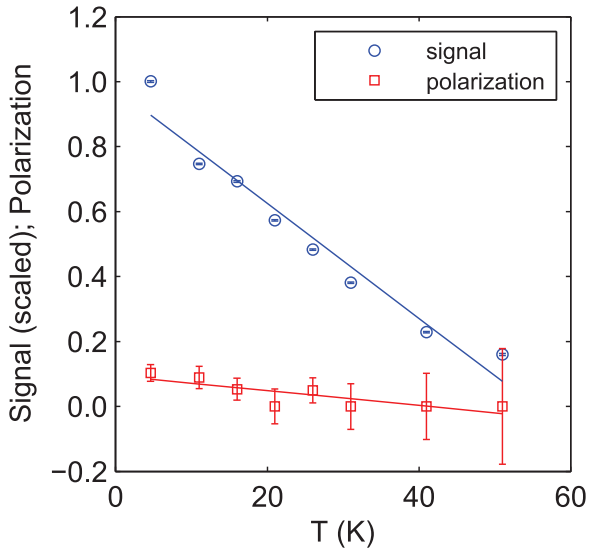

FIG. 1. (Color online) Plot of normalized ^{31}P NMR signal amplitude (blue circles) and nuclear polarization (red squares), defined as $\langle I_z \rangle / I$, vs temperature for 800 s irradiation with σ_+^B light at 1.428 eV.

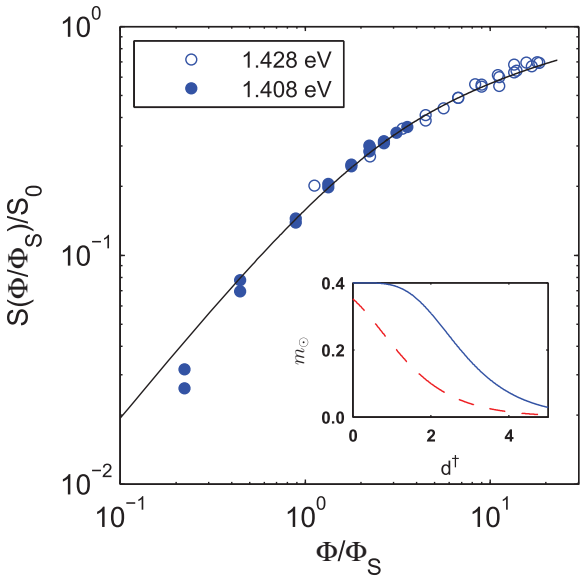

FIG. 2. (Color online) Plot of normalized ^{31}P NMR signal amplitude as a function of laser power normalized to the saturation laser power. The signals (open circles, 1.428 eV; filled circles, 1.408 eV) were obtained by illuminating the sample for 200 s with σ_+^B light. The normalization parameters were obtained by fitting the data to the integral over $d^\dagger$ of Eq. (16). The saturation parameters Φ_S are 0.3 and 1.6 W/cm^2 at 1.428 and 1.408 eV, respectively. Inset: Polarization as a function of normalized depth, from Eq. (16), for Φ/Φ_S of 2 (dashed red line) and 11 (solid blue line) corresponding to the typical experimental situation 3.4 W/cm^2 pumping power for 1.408 and 1.428 eV, respectively.

These values indicate that sample heating by a few K from irradiation would not have a large effect on the measured signal amplitude or nuclear polarization.

Previous studies of optical pumping in Fe-doped semi-insulating InP (Showa Denko, carrier concentration 7×10^7 cm^{-3}) at 6.3 T found that the temperature dependence of the signal intensity was very photon-energy dependent [6,10,42]. The ^{31}P signal disappeared above 20 K at all photon energies except near 1.407 eV (sub-bandgap), where the signal was observed to persist above 50 K. In contrast, Fig. 1 shows that the ^{31}P signal persists to above 50 K above the band gap (1.428 eV) at 2.35 T. Presumably, this is a consequence of the difference in band structure at the two fields [23]. It suggests that, in addition to the observed faster cross-relaxation rate [7], lower magnetic fields may provide a more favorable temperature dependence for optical pumping in the photon-energy regime desired for high surface polarization.

B. Light intensity dependence

Equation (16) predicts that above a certain incident light power, the signal amplitude will not increase linearly with increased light intensity. This effect is demonstrated in Fig. 2, where normalized signal amplitude as a function of light power normalized to the saturation light power is plotted. Data were obtained for absolute light intensities spanning the range 0.3–7 W/cm^2. For sub-bandgap irradiation the signal grows nearly linearly with laser power, whereas super-bandgap irradiation results in markedly nonlinear growth. The saturation parameters Φ_S were obtained by fitting the data to Eq. (16) integrated over $d^\dagger$: $S(\Phi/\Phi_S) = \int m_\odot(\Phi, d^\dagger) dd^\dagger$. The saturation light powers are 0.3 and 1.6 W/cm^2 at 1.428 and 1.048 eV, respectively. Our value at 1.428 eV is similar to our smallest applied power, and comparable to the value for undoped InP (0.1 W/cm^2) [11]. The higher value of Φ_S at 1.408 eV is consistent with the reported greater optical penetration depth below band gap [5].

C. Frequency shifts

As shown in Fig. 3, we compared spectra from data taken with light on during acquisition and the light off during acquisition for short pumping times. As a function of pumping power, "light-off" spectra were very similar in central frequency and shape both for sub- and super-bandgap irradiation. The "light-on" spectra were shifted in frequency and broadened compared to the "light-off" spectra, particularly at short pumping times. These spectral differences are due to the polarized electron.

It was with this in mind that we studied the change in the spectra with pumping time τ_L. In order to isolate just the contribution to the spectra from the hyperfine coupling, we simultaneously fit all of the light-on $S_{\rm on}$ and light-off $S_{\rm off}$ complex data in time t to the following functions:

$$S_{\rm off}(\tau_L) = S_0(\tau_L) \exp\left(-\left\{t^2/\left(2T_G^2\right) + t/T_{2e}\right\}\right) \times \exp(i\{2\pi f_{\rm off} t + \phi\}), \quad (22)$$

$$S_{\rm on}(\tau_L) = S_{\rm off} \exp(-i2\pi \Delta f t) \exp(-t\Gamma), \quad (23)$$

where T_{2e} is the exponential decay constant characteristic of T_2 processes, T_G is the Gaussian decay constant characteristic of T_2^* that defines the echo envelope shape, Γ is the

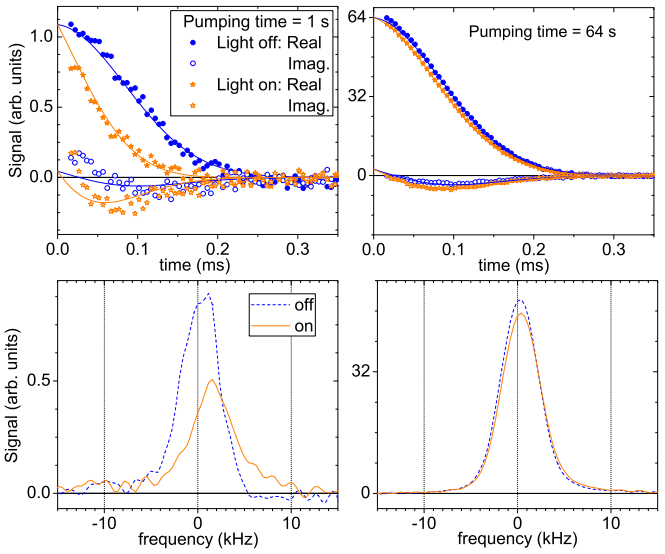

FIG. 3. (Color online) The top two graphs show complex ^{31}P NMR echo data starting with the midpoint of the echo and the graphs below give the corresponding spectra; for clarity only the real spectral data are shown. For long pumping time data, as shown in the rightmost graphs, the signals are very similar for data acquired with the laser light off (blue circles) and on (orange stars). In contrast, for short pumping time data, as shown in the leftmost graphs, the light-on signal decays more quickly than the light-off signal and is shifted in frequency, revealing the effects of the polarized electron. While the data shown here are for sub-bandgap irradiation, super-bandgap irradiation shows similar trends. The solid lines in the upper graphs correspond to fits to the data, as described by Eqs. (22) and (23).

additional light-induced broadening, and $\Delta f \equiv f_{\rm off} - f_{\rm on}$ is the frequency shift due to hyperfine coupling. For the light-off data we found the Gaussian time constant, $T_G = 90 \pm 1$ μs for sub-bandgap and $T_G = 84 \pm 1$ μs for super-bandgap pumping, dominates the decay behavior; the exponential decay constant, $T_{2e} = 1.4 \pm 1.0$ ms (sub-bandgap) and $T_{2e} = 1.7 \pm 1.1$ ms (super-bandgap), makes little, if any, contribution to the decay.

Using the results of fitting the spectra to Eqs. (22) and (23), we compare the dependence of Δf and Γ to numerical solutions to Eq. (4). To facilitate the numerical solution to Eq. (4), we calculate $D = 3.3$ nm^2/s for the particular orientation of our single crystal in the magnetic field [28]. For J_z we choose to use the lower limit of -0.15 obtained from Eq. (2) and $I_\infty = -0.07$ (see Sec. IV D); we will find that the choice of J_z does not have a large effect on our results. $T_{1L}(0)$ is not expected to contribute to the signal evolution at these short pumping times and is set to an arbitrarily long time of 5000 s.

As shown in Fig. 4 (bottom and middle plots), for longer pumping times most of the polarized nuclei are far from the polarized electron so that both frequency shifts and broadening are greatly diminished. The black line in the bottom plot represents the calculated absolute first moment of the line shape for our super-bandgap data, obtained from Eqs. (4), (19), and (20). The best fit of the temporal evolution of the first moment of the line shape from Eq. (4) to Δf, super-bandgap, is obtained with $a_0 = 6$ nm and $F = 0.02$,

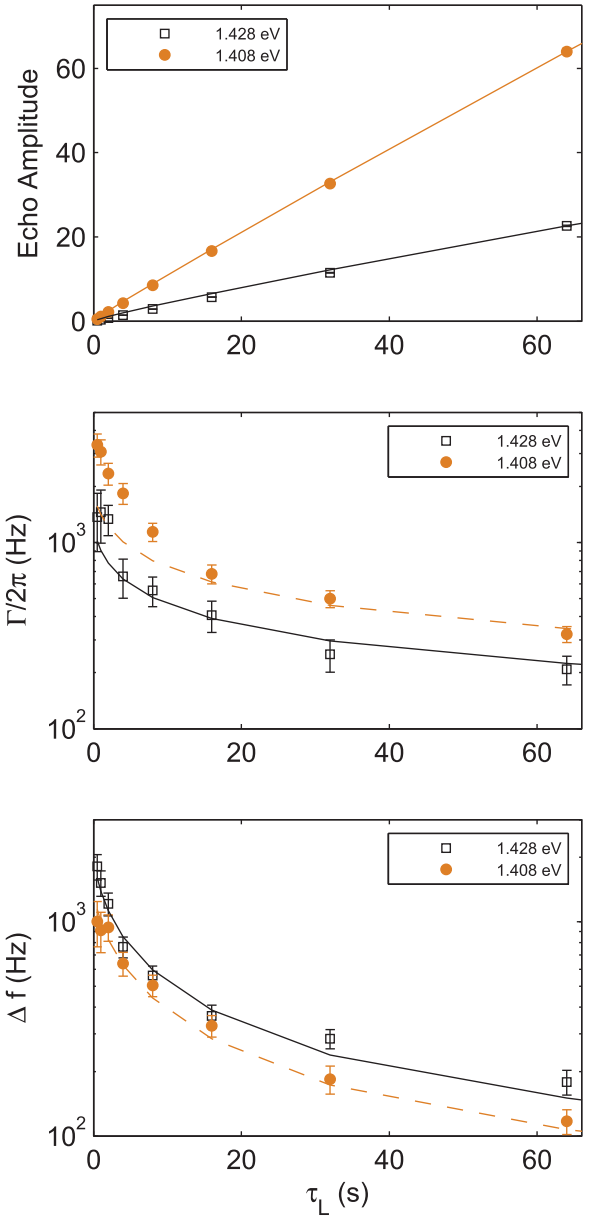

FIG. 4. (Color online) Plots of ^{31}P NMR spectral data as a function of pumping time for sub-bandgap data (orange filled circles) and super-bandgap data (black open squares). The lines, from top plot to bottom plot, represent scaled nuclear polarization, scaled square root of the second moment of the line shape ($\div 2$ super-bandgap, $\times 2$ sub-bandgap), and absolute first moment of the line shape ($\times 2$ sub-bandgap), respectively, obtained from the model. As shown in the top figure the amplitude of the echo signal is linear with pumping time. In contrast, for pumping times on the order of 20 s or less, the spectral behavior changes quite dramatically as a function of pumping time. The narrowing of the spectral line with pumping time is demonstrated in the middle graph, while the bottom graph shows how Δf decreases for increasing τ_L. While sub-bandgap data and super-bandgap data show similar behavior, the broadening, defined as $\Gamma/(2\pi)$, for sub-bandgap behavior is more pronounced.

resulting in $f_0 = 8.1$ kHz and $T_{1C}(0,0) = 0.20$ s. (The choice of J_z has only a modest effect on the parameters: increasing J_z to -0.3 increases $T_{1C}(0,0)$ by roughly a factor of 2 and leaves

a_0 unchanged.) In the middle plot the black line represents the square root of the second moment of the calculated NMR line shape (super-bandgap). We note that the second moment of the function chosen for the light-induced broadening in Eqs. (22) and (23) does not converge to a finite value. The square root of the calculated second moment is reduced by a factor of 2 to show the qualitative agreement between the results of Eqs. (4) and (21) and the measured data, particularly with regard to the linewidth. The amplitude of the echo signal $S_0(\tau_L)$ (top plot) scales linearly with τ_L, consistent with an exponential recovery curve with a long time constant as observed experimentally. The lines represent the calculated scaled integrated fractional nuclear polarization obtained from Eq. (4). Calculating signal amplitude requires accurate knowledge of d_0 as a function of photon energy.

We also compare spectral results to numerical solutions to Eq. (4) for our sub-bandgap data in Fig. 4. The differences in the numerical solutions sub- and super-bandgap arise from differences in the saturation factor and light intensity as they enter Eq. (19). The measured values of Δf, sub-bandgap, are larger than the values of the first moment obtained from Eq. (4): the dashed line in the plot is scaled by a factor of 2 to show that the numerical solution predicts the correct time dependence of Δf. Likewise, the measured values of the linewidth, sub-bandgap, are larger than the values of the square root of the second moment: the dashed line is scaled by a factor of 4 relative to the values calculated for super-bandgap.

It should be noted that the intensity of light for the two experiments was quite different. Using the definition $\Phi = P/(\pi w^2)$, where P is the optical power and w is the waist of the pump beam, $\Phi_{\text{sub}} = 2$ W/cm^2 and $\Phi_{\text{super}} = 7$ W/cm^2. Looking at the signal versus pump power (Fig. 2) leads us to conclude that we are operating in a saturated regime for super- and sub-bandgap irradiation, although we are further into the saturated regime for the super-bandgap irradiation. Data taken with the same intensity light, 4 W/cm^2, and the same pumping time of a half second show a similar net light shift for sub- and super-bandgap irradiation; this is in contrast to the data in Fig. 4 where the light shift is larger for super-bandgap irradiation.

One can observe that while light broadening under sub-bandgap irradiation is significantly larger than under super-bandgap irradiation, the central frequency shift is smaller. In fact, for sub-bandgap irradiation the broadening is larger than the central frequency shift. This unusual feature indicates that there is another broadening mechanism at work for sub-bandgap irradiation, one that adds broadening but not a shift, such as the broadening due to the noncontact dipolar coupling interaction, as discussed in more detail in the Appendix. It is observed for sub-bandgap irradiation, where the broadening is the greatest, that the broadening monotonically increases with decreasing pumping time, while the central frequency plateaus. This is indicative of the wave function for the relevant ORD in sub-bandgap irradiation deviating from the $1s$ electron wave function; in particular the electronic density is more localized around the ORD than in the case of super-bandgap irradiation. Such tight localization would correspond to "deeper" trap sites. The existence of deep trap sites serving as ORDs has been observed in GaAs [43].

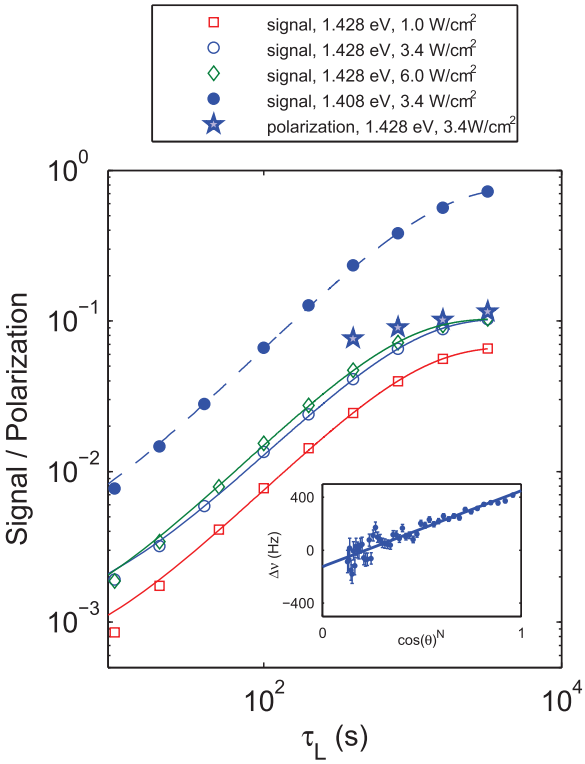

FIG. 5. (Color online) The ^{31}P NMR signal grows with irradiation time; the nuclear polarization, defined as $\langle I_z \rangle / I$, grows at an even faster rate. Sub-bandgap (blue filled circles) irradiation leads to slower signal buildup compared to super-bandgap (blue open circles), for the same power, 3.4 W/cm^2. Higher power irradiation, 6 W/cm^2 (green triangles), results in faster buildup and lower power irradiation, 1 W/cm^2 (red squares), results in slower buildup of signal. Signal-weighted polarization buildup for super-bandgap irradiation at 3.4 W/cm^2 is plotted as shaded blue stars. The signal (normalized) and polarization share the same axes. Inset: Plot of the resonance frequency difference between signals from irradiation with σ_+^B and σ_-^B light vs total pulse angle for 3200-s irradiation time at 3.4 W/cm^2. The slope of the line gives an initial signal-weighted polarization of 12%.

D. Signal amplitude and polarization as a function of pumping time and light intensity

Signal amplitude was measured for τ_L in the range 1–3200 s sub-bandgap at 3.4 W/cm^2, and super-bandgap at 1.0, 3.4, and 6.0 W/cm^2. Polarization was measured for pumping times in the range 400–3200 s super-bandgap at 3.4 W/cm^2, with both light helicities. Experimentally, we find that signal amplitude data (Fig. 5) fit well to exponential recovery curves such as Eq. (13), which is given for a single sphere of influence. The time constant $\mathcal{T}_B$, obtained from fitting the signal amplitude, comes from a signal-weighted average of all the spheres of influence, and is not simply related to the time constants $T_B(d^\dagger)$. The signal amplitude time constants for 1.428 eV light and 1.0, 3.4, and 6.0 W/cm^2 are 890 ± 10, 820 ± 10, and 670 ± 10 s, respectively. We observe that $\mathcal{T}_B$ decreases with increasing Φ, as expected based on Eq. (18). We also observe that S increases with increasing Φ, and that the saturation effect appears more pronounced at longer pumping times. For 1.408 eV light at 3.4 W/cm^2 the time constant is 1170 ± 30 s,

longer than the values for super-bandgap irradiation, as expected based on Eq. (18). Over the range of times the polarization was measured the temporal evolution is almost flat; therefore, it is not possible to obtain a reliable time constant for the polarization evolution, although clearly the buildup time is shorter than that for the signal under identical conditions.

From fitting our data to exponential recovery curves (Fig. 5) we observe that the time constant $\mathcal{T}_B$ is 1.4 times longer at 1.408 eV, compared to 1.428 eV. Equation (18) relates $1/T_B$ at depth $d^\dagger$ to light intensity. Our measured value of $1/\mathcal{T}_B$ is averaged over all $d^\dagger$:

$$\frac{1}{\mathcal{T}_B} \propto \frac{\int_0^\infty m_\odot(\Phi,d^\dagger)^2 dd^\dagger}{\int_0^\infty m_\odot(\Phi,d^\dagger) dd^\dagger}, \tag{24}$$

for small τ_L. We note that Eq. (24) is independent of d_0. We can calculate the ratio of the buildup time constants at 1.428 and 1.408 eV by numerically evaluating Eq. (24) at each energy, obtaining a value of 1.5, in good agreement with our measured value of 1.4.

Our method of measuring polarization relies on the development of a polarized disk. Above a certain thickness threshold, the thickness of the disk does not greatly affect the determination of polarization. If the growth of polarization is faster closer to the surface than farther into the InP, then a polarized disk will develop that grows in thickness. Once the threshold thickness is exceeded, the polarization will stop "growing" even while the signal amplitude continues to grow. Additional signal growth after this time occurs deeper in the InP.

Equation (4), in combination with Eqs. (19) and (20), suggests that a single set of parameters can be used to fit the signal buildup data as a function of time, light intensity, and photon energy. Based on the short pumping time frequency-shift results, for a given value of J_z, we obtain values of $T_{1C}(0,0)$ and F; we showed earlier that $\Phi_S = 0.3$ W/cm^2 at 1.428 eV and 1.6 at 1.408 eV. We integrate over the range $0 \leqslant d^\dagger \leqslant 5$. Signal and polarization are then modeled with parameters in the range $1 \leqslant r^*_{\max} \leqslant 15$, $100\text{ s} \leqslant T_{1L}(0) \leqslant 3000$ s, and $-0.30 \leqslant J_z \leqslant -0.15$. The model predicts that the polarization (and signal) build up most rapidly near the surface of the InP and more slowly at greater depths. Therefore, we assume that the polarization values are dominated by the near surface region, which we define as $d^\dagger \leqslant 1$.

A set of signal buildup curves was calculated for 1.428 eV light with intensities of 1.0, 3.4, and 6.0 W/cm^2. Signal buildup data for each of the three laser intensities were scaled and compared to the buildup curves by calculating least-squares residuals. The residuals for 3.4 W/cm^2 light intensity and $J_z = -0.15$ are plotted in Fig. 6. The minima in the residuals follow an "L"-shaped trough outlined by the red contour lines. The "vertical" part of the L is centered around $r^*_{\max} \approx 5$ and is independent of $T_{1L}(0)$. The "horizontal" part of the L is centered around $T_{1L}(0) \approx 500$ s and is almost independent of $r^*_{\max}$. The transition region between the "horizontal" and "vertical" regions is sensitive to both $T_{1L}(0)$ and $r^*_{\max}$. Plots of the residuals for other laser intensities and values of J_z (not shown) are similar to Fig. 6, with the "vertical" region centered at $r^*_{\max} \approx 5$ and the "horizontal" region centered around $T_{1L}(0) \approx 500$ s. The shape of the minima in the residuals describes two limiting cases for the signal buildup.

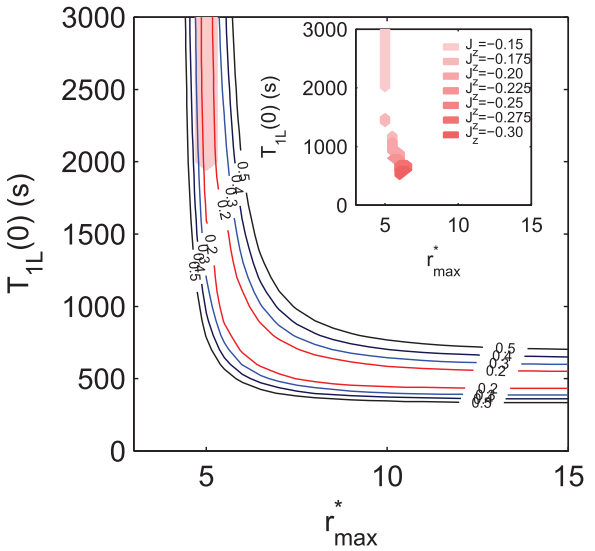

FIG. 6. (Color online) Plot of least-squares residuals between the signal buildup model [Eq. (4)] and measurements of ^{31}P NMR signal amplitude for 1.428 eV irradiation at 3.4 W/cm^2 as a function of $r^*_{\max}$ and $T_{1L}(0)$ for $J_z = -0.15$. The area between the red contours is the area of minimum residuals. The shaded area is the region where the model predicts nuclear polarization between 10% and 14%, for 3200 s of irradiation at 1.428 eV, consistent with the measured value (Fig. 5). Inset: The shaded regions are where the model predicts nuclear polarization between 10% and 14%, for 3200 s of irradiation at 1.428 eV for several values of J_z. The value of $r^*_{\max}$ remains between 5 and 6 for all values of J_z.

In the "vertical" region of the trough the buildup time constant is determined by the time it takes to fully polarize the sphere of influence around the ORD, whereas the buildup time constant in the "horizontal" region is limited by $T_{1L}(0)$ and results in lower polarization.

The signal buildup behavior alone cannot distinguish between the two limiting cases which determine the buildup time constant; however, polarization buildup may separate the two cases. We calculate polarization from the model by summing over the region $d^\dagger \leqslant 1$. We model the polarization for $\Phi = 3.4$ W/cm^2 and $\tau_L = 3200$ s, looking for polarization values between 10% and 14%, as determined by the data in Fig. 5. The shaded region of Fig. 6 meets the criterion for nuclear polarization between 10% and 14%. The shaded region clearly shows that the signal buildup cannot be limited by $T_{1L}(0)$ for $J_z = -0.15$. For larger absolute values of J_z the region where nuclear polarization values fall between 10% and 14% shifts toward lower values of $T_{1L}(0)$ (inset to Fig. 6) but remains close to a value of 5 for $r^*_{\max}$.

In Fig. 6, the innermost contours (shown in red) bound the region where the residual is less than or equal to two times the minimum residual. In this region we fitted the calculated buildup curves to Eq. (13) to find $\mathcal{T}_B$ to be 920 ± 50, 740 ± 30, and 670 ± 20 s for light intensities of 1.0, 3.4, and 6.0 W/cm^2, respectively, consistent with the data of Fig. 5. The model also predicts polarization buildup time constants for the three light intensities of 440 ± 2, 440 ± 10, and 460 ± 3 s, respectively.

With $r^*_{\max} = 5$ determined from the temporal evolution of signal and polarization, and $a_0 = 6$ nm, we could estimate the

average distance between ORDs, $2r_{\max}$. However, the value of $r^*_{\max}$ also depends on D^*, which has not been determined experimentally for InP. The value $D^* = 0.092\ \mathrm{s}^{-1}$ used above was calculated using the method of Khutsishvili [28], and is broadly consistent with estimates of D based on the ^{31}P-^{31}P homonuclear dipolar second moment [44]. In the limit $\sqrt{\mathcal{T}_B D} \gg a_0$, spatial evolution of nuclear polarization is driven by spin diffusion, resulting in

$$r^*_{\max} \propto \sqrt{\mathcal{T}_B D^*}, \tag{25}$$

therefore estimates of $r_{\max}$ depend only on the square root of D. For $r^*_{\max} = 5$ we find $2r_{\max} \approx 60$ nm, leading to a number density of ORDs of $5 \times 10^{15}\ \mathrm{cm}^{-3}$, which is not unreasonable given the typical shallow donor concentrations in similarly prepared InP materials [45].

We can compare our experimental super-bandgap results at 2.35 T to published results from the same sample at 9.4 T [5] by using the model to fit an exponential recovery curve with the reported time constant of 4090 s. Scaling $T_{1C}(0,0)$ by a factor of 15.2 [Eq. (7)], a plot of the residuals as a function of $T_{1L}(0)$ and $r^*_{\max}$ (not shown) again has an L-shaped minimum trough with the "vertical" region centered about $r^*_{\max} \approx 4$, similar to the results at 2.35 T. The intersection of the "horizontal" and "vertical" sections of the trough occurs around $T_{1L}(0) \approx$ 3600 s at 9.4 T compared to 500 s at 2.35 T (Fig. 6). The ratio of these values is 7.2, comparable to the predicted value of 5.8 [Eq. (9)].

We have also applied the signal buildup model to data obtained at 1.408 eV and 3.4 W/cm^2 irradiation, using the same parameters as for the 1.428 eV data adjusted for the different light saturation parameters. This choice is justified by the close similarity in the time evolution of the hyperfine shift sub- and super-bandgap (Fig. 4). The shape of the residuals surface (not shown) is qualitatively the same as that in Fig. 6: the region of minimum residuals is L shaped with the vertical region at $r^*_{\max} \approx 5$, and the horizontal region at $T_{1L}(0) \approx 500$ s. The nuclear polarization sub-bandgap is too small for us to measure directly; therefore, either J_z is a much smaller sub-bandgap than it is super-bandgap, or signal buildup is limited by T_{1L} for sub-bandgap irradiation. However, a large difference in J_z would seem to be at odds with the observed similarity in the magnitudes of the hyperfine shifts at the two photon energies (Fig. 4). Having a large change in J_z while maintaining similar hyperfine shifts would require an offsetting large change in F.

If the values of J_z and F are similar sub- and super-bandgap, the growth of signal must be limited by T_{1L}. This, in turn, argues that the magnitude of J_z must be large to account for the significant steady-state nuclear polarization under super-bandgap irradiation. Then, the large difference in steady-state nuclear polarization sub- and super-bandgap arises from differences in $r^*_{\max}$. A larger $r^*_{\max}$ would be consistent with only a subset of ORD's being accessible under sub-bandgap irradiation.

V. CONCLUSIONS

We have obtained OPNMR data for InP for two photon energies, sub- and super-bandgap, as a function of pumping time from less than 1 s to nearly 1 h. For short pumping times we acquired ^{31}P NMR data with and without light irradiation during the acquisition to gain insights into the initial buildup mechanism. For longer pumping times we acquired data as a function of laser power to gain insights into saturation effects and the propagation of polarization through the sample.

We use a simple model in which optical pumping creates spin-polarized electrons which become trapped at ORDs. The buildup of polarization within the material is then described by a single master equation, Eq. (4), containing terms associated with cross relaxation, spin diffusion, and spin-lattice relaxation. We also make use of two additional phenomenological equations: (i) the OPNMR polarization buildup at times longer than a few seconds follows the functional form of exponential recovery with time constant T_B, and (ii) OPNMR signal as a function of light intensity follows Eq. (16), proposed by Tycko. All of our OPNMR data were analyzed by solving these fundamental equations numerically.

The OPNMR data for pumping times τ_L less than 100 s acquired with and without light during acquisition revealed large spectral shifts and broadening due to the polarized electrons nearby those nuclei which had been polarized via cross relaxation. From the magnitude of the frequency shift as τ_L approaches zero, we put a lower limit on $f_0(0)$, the maximum frequency shift of a ^{31}P nucleus, of 8.1 kHz for super-bandgap irradiation. Fitting the time evolution of the hyperfine shift to our model, for $J_z = -0.15$, we calculate the Bohr radius a_0 of the ORD to be 6 nm, and the fractional occupancy F to be 0.02. Further analysis gives the cross-relaxation time $T_{1C}(0,0) = 0.2$ s. For fits to our super-bandgap hyperfine shift data, in the range $-0.30 \leqslant J_z \leqslant -0.15$, F and $1/T_{1C}(0,0)$ are inversely proportional to J_z; a_0 is independent of J_z. While our model fits the super-bandgap data quite well, there is a significant discrepancy for the sub-bandgap data where we observe larger-than-expected broadening and shifts, although the model does reproduce the temporal evolution of the shifts. A possible explanation is a more localized nonhydrogenic electron density for the ORDs in a deeper level associated with sub-bandgap cross relaxation.

From the longer pumping time super-bandgap OPNMR data, using parameters determined from the short pumping-time analysis, $T_{1C}(0,0)$ in particular, we determine that the number density of accessible ORDs super-bandgap, $5 \times 10^{15}\ \mathrm{cm}^{-3}$, is insensitive to the value of J_z. Again the sub-bandgap results, where the polarization density is significantly smaller, are more difficult to interpret. Nevertheless, for long optical pumping times, the differences in the optical saturation factors derived from Eq. (16) provide a reasonable explanation for the differences in the signal buildup time constants sub- and super-bandgap. Assuming J_z, F, and a_0 are similar sub- and super-bandgap, as suggested by the hyperfine shift results, our results are consistent with the buildup being limited by the spin-lattice relaxation time T_{1L} and the lower steady-state nuclear polarization under sub-bandgap irradiation arising from a larger $r_{\max}$. This argument does not take into consideration the localized nonhydrogenic electron density for ORDs sub-bandgap; however, if the localized electron density falls well inside the radius at which spin diffusion becomes the dominant mechanism for polarizing nuclei, polarization of the bulk of the nuclei will come from cross relaxation in the wings of the electron distribution which may be more hydrogenic in

nature. This slower cross-relaxation process could reduce the overall nuclear polarization.

Our study of the buildup of OPNMR in InP provides a deeper understanding of the physical parameters which underlie the buildup process. It should be emphasized that the parameters derived from the numerical solutions to Eq. (4) depend strongly on the value of a_0, determined using our calculated value of the spin-diffusion constant. Our results confirm that super-bandgap irradiation is most effective at creating high nuclear polarizations near the surface. Achieving high polarizations at the surface, as is necessary for polarization transfer from the semiconductor to another material, will require control of these parameters via a better understanding of the true nature of the ORDs.

ACKNOWLEDGMENTS

We wish to thank Dr. R. Tycko for providing the Fe-doped InP sample used in these studies, Dr. S. Hart for the use of his lasers, and Professor G. Miller for help with probe construction. This work was supported by the Office of Naval Research.

APPENDIX: CONTACT AND NONCONTACT FREQUENCY SHIFTS

To understand the relative contribution to the frequency shifts from the contact and noncontact coupling, we treat the problem as one of finding the magnetic field from a smooth magnetization distribution $\mathbf{M} = -g\mu_B F\langle\mathbf{J}\rangle n$, where n is the trapped electron probability density around an ORD. Taking n as radially symmetric, we can build up $\mathbf{M}$ as a series of magnetized spheres and shells; using the principle of superposition we can sum their field contributions to get the field at a particular location. At a given radius r', we model the magnetic field as coming from (1) a sphere of uniform magnetization of value $\mathbf{M}(r')$ and extending to a radius $R = r' + dr/2$, (2) uniformly magnetized spherical shells of thickness dr with radii $R < r < \infty$; by symmetry each of these shells contributes no field at r', (3) a series of uniformly magnetized spheres with radii $r < (r' - dr/2)$. The magnetic field from the last is equivalent to that from a single magnetic dipole $\mathbf{m}$ centered at the origin,

$$\mathbf{m}(\mathbf{r}') = -g\mu_B F\langle\mathbf{J}\rangle \int_0^{r'-dr/2} [n(r) - n(r')]d^3r \qquad \text{(A1)}$$

with the corresponding field

$$\mathbf{B}_d(r') = \frac{\mu_0}{4\pi}\left(\frac{3\mathbf{r}'(\mathbf{r}'\cdot\mathbf{m})}{r'^5} - \frac{\mathbf{m}}{r'^3}\right). \qquad \text{(A2)}$$

Note that this term is anisotropic. Only the z component of the field, along the direction of the main field, will contribute to the broadening of the spectrum. Also taking $\mathbf{m} = m_z\hat{z}$, or $\langle\mathbf{J}\rangle = \langle J_z\rangle\hat{z}$, we find

$$\mathbf{B}_d \cdot \hat{z} = \frac{\mu_0 m_z(r')}{4\pi}\frac{3\cos^2\theta - 1}{r'^3}, \qquad \text{(A3)}$$

where $\cos\theta$ is the directional cosine between $\mathbf{r}'$ and $\hat{z}$. With $\int(3\cos^2\theta - 1)d\Omega = 0$, and assuming isotropic nuclear polarization, there would be no net shift due to this contribution; there would however be a broadening of the spectrum.

Now the only remaining contribution to the magnetic field at r' is from the sphere with uniform magnetization $\mathbf{M}(r')$. This sphere is representative of the contact, or hyperfine, interaction. However, on a microscopic level it must be considered that in fact the electron probability density is not smooth; rather the electron is to be found preferentially close to the nuclei; the associated degree of localization [26] for ^{31}P in InP is $\rho v_0 = 6.6 \times 10^3$. Therefore the contact field is

$$\mathbf{B}_{\text{contact}}(r') = -\tfrac{2}{3}\mu_0 g\mu_B F\langle J_z\rangle[\rho v_0 n(r')]\hat{z}. \qquad \text{(A4)}$$

This field is isotropic and negative for all possible values of r'. Under the influence of this field, the spectrum would shift downwards and broaden, but in such a way that the distribution contains only negative frequency shifts. This is in contrast to the dipole field in which negative and positive frequency shifts are expected.

To compare the two effects' strength, we can examine the ratio $\frac{B_d}{B_{\text{contact}}}$ at the angle at which the dipole field is the strongest, $\theta = 0^\circ$, as a function of r' and in the limit that dr' approaches zero,

$$\frac{B_d(r')}{B_{\text{contact}}(r')} = \frac{1}{\rho v_0}\left[\frac{\int_0^{r'}\left(\frac{n(r)}{n(r')} - 1\right)d^3r}{4\pi r'^3/3}\right], \qquad \text{(A5)}$$

where the expression in square brackets represents the average deviation of the smoothed electron probability density within $r < r'$ from the density at $r = r'$. For large values of r',

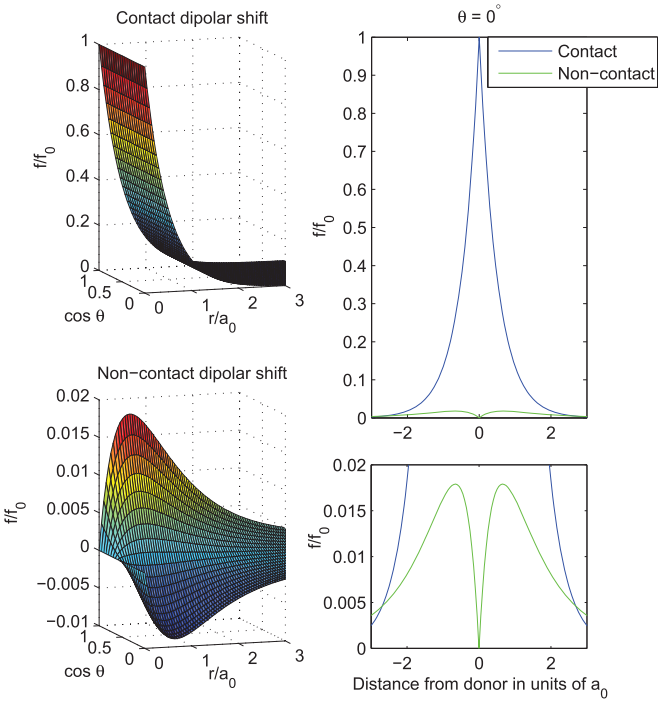

FIG. 7. (Color online) The left set of graphs shows the frequency shift in terms of f_0 expected at a given radius r/a_0, and $\cos\theta$, for contact dipolar interaction (top) and noncontact interaction (bottom). The right graph shows a comparison of the two shift contributions for $\theta = 0$.

the dipolar term will dominate. The radius at which this occurs depends on the exact nature of the electron probability distribution.

For a 1s electron probability density, as is associated with a shallow donor,

$$n(r) = \frac{1}{\pi a_0^3} e^{-2r/a_0}. \tag{A6}$$

The frequency shifts for both the contact and noncontact fields are show in Fig. 7, for ^{31}P in InP. For radii less than $2a_0$, the contact field clearly dominates.

For a "deep" trapping site the electron distribution may have a significant fraction in the central cell [46]. We estimate such a distribution as

$$n = \frac{\alpha}{\pi a_0^3} e^{-2r/a_0} + \frac{(1-\alpha)}{\pi b_0^3} e^{-2r/b_0}, \tag{A7}$$

where b_0 is on the order of the central cell, $a_0 \gg b_0$, and α gives the relative weighting of the two distributions. The net effect of having a more localized distribution would be to effectively reduce the filling factor by α, since the more localized distribution would not contribute to the cross relaxation. For $b_0 \ll r' < a_0$ and $\theta = 0^\circ$

$$\frac{B_d(r',\theta=0^\circ)}{B_{\text{contact}}(r')} = \frac{3}{4\rho v_0} \frac{a_0^3}{r'^3} \frac{(1-\alpha)}{\alpha}. \tag{A8}$$

For sub-bandgap irradiation we see in Fig. 4 a ratio of broadening to shift, $\Gamma/(2\pi\,\Delta f)$, of 1.7, as opposed to the super-bandgap irradiation where the same ratio is 0.4. These ratios are for the shortest pumping time observed, $\tau_L = 1/2$ s, when the nuclear polarization would have limited spatial extent. The relatively large sub-bandgap ratio could be explained by a small α, that is a large fraction of the electron probability is highly localized around the ORD. For instance if the spatial extent is limited to $a_0/6$ and $\alpha = 0.02$, the ratio of $\frac{B_d(a_0/6,\theta=0^\circ)}{B_{\text{contact}}(a_0/6)}$ would be 1.2. This value can be be compared to $\Gamma/(2\pi\,\Delta f) = 1.7$ where the broadening is taken as a metric of the noncontact interaction and the shift as a metric of the contact interaction.

[1] M. I. Dyakonov and V. I. Perel, *Optical Orientation*, edited by F. Meier and B. P. Zakharchenya (North-Holland, Amsterdam, 1984).
[2] R. Tycko and J. A. Reimer, J. Phys. Chem. **100**, 13240 (1996).
[3] S. E. Hayes, S. Mui, and K. Ramaswamy, J. Chem. Phys. **128**, 052203 (2008).
[4] J. A. Reimer, Solid State Nucl. Magn. Reson. **37**, 3 (2010).
[5] C. A. Michal and R. Tycko, Phys. Rev. B **60**, 8672 (1999).
[6] K. Hashi, A. Goto, R. Miyabe, T. Shimizu, G. Kido, S. Ohki, and S. Machido, Physica B **329-333**, 1235 (2003).
[7] K. L. Sauer, C. A. Klug, J. B. Miller, and J. P. Yesinowski, Phys. Rev. B **84**, 085202 (2011).
[8] A. Patel, O. Pasquet, J. Bharatam, E. Hughes, and C. R. Bowers, Phys. Rev. B **60**, R5105 (1999).
[9] C. A. Michal and R. Tycko, Phys. Rev. Lett. **81**, 3988 (1998).
[10] A. Goto, K. Hashi, T. Shimizu, R. Miyabe, X. Wen, S. Ohki, S. Machida, T. Iijima, and G. Kido, Phys. Rev. B **69**, 075215 (2004).
[11] R. Tycko, Solid State Nucl. Magn. Reson. **11**, 1 (1998).
[12] L. Goehring and C. A. Michal, J. Chem. Phys. **119**, 10325 (2003).
[13] D. Paget, Phys. Rev. B **25**, 4444 (1982).
[14] P. J. Coles and J. A. Reimer, Phys. Rev. B **76**, 174440 (2007).
[15] K. Ramaswamy, S. Mui, and S. E. Hayes, Phys. Rev. B **74**, 153201 (2006).
[16] S. Mui, K. Ramaswamy, and S. E. Hayes, Phys. Rev. B **75**, 195207 (2007).
[17] P. L. Kuhns, A. Kleinhammes, T. Schmiedel, W. G. Moulton, E. Hughes, S. Sloan, P. Chabrier, and C. R. Bowers, Phys. Rev. B **55**, 7824 (1997).
[18] S. Mui, K. Ramaswamy, and S. E. Hayes, J. Chem. Phys. **128**, 052303 (2008).
[19] C. Weisbuch and C. Hermann, Phys. Rev. B **15**, 816 (1977).
[20] C. Weisbuch and C. Hermann, Solid State Commun. **16**, 659 (1975).
[21] M. Oestreich, S. Hallstein, A. P. Heberle, K. Eberl, E. Bauser, and W. W. Rühle, Phys. Rev. B **53**, 7911 (1996).
[22] P. J. Coles, Phys. Rev. B **78**, 033201 (2008).
[23] K. Ramaswamy, S. Mui, S. A. Crooker, X. Pan, G. D. Sanders, C. J. Stanton, and S. E. Hayes, Phys. Rev. B **82**, 085209 (2010).
[24] N. Bloembergen, Physica **15**, 386 (1949).
[25] A. Abragam, *The Principles of Nuclear Magnetism* (Clarendon, Oxford, 1961).
[26] N. T. Bagraev and L. S. Vlasenko, Sov. Phys. Solid State **21**, 70 (1979).
[27] J. Lu, M. J. R. Hoch, P. L. Kuhns, W. G. Moulton, Z. Gan, and A. P. Reyes, Phys. Rev. B **74**, 125208 (2006).
[28] G. R. Khutsishvili, Sov. Phys. Usp. USSR **8**, 743 (1966).
[29] M. I. D'yakonov and V. I. Perel', JETP **38**, 177 (1974).
[30] B. Gotschy, G. Denninger, H. Obloh, W. Wilkening, and J. Schneider, Solid State Commun. **71**, 629 (1989).
[31] D. Paget, G. Lampel, B. Sapoval, and V. I. Safarov, Phys. Rev. B **15**, 5780 (1977).
[32] P. Y. Yu and M. Cardona, *Fundamentals of Semiconductors: Physics and Materials Properties*, 4th ed. (Springer-Verlag, Berlin, Heidelberg, 2010).
[33] *Landolt-Börnstein - Group III Condensed Matter: Group IV Elements, IV-IV and III-V Compounds. Part b - Electronic, Transport, Optical and Other Properties*, V. 41A1b, edited by O. Madelung, U. Rossler, and M. Schulz (Springer, Berlin, Heidelberg, 2002).
[34] W. Farah, M. Dyakonov, D. Scalbert, and W. Knap, Phys. Rev. B **57**, 4713 (1998).
[35] N. W. Ashcroft and N. D. Mermin, *Solid State Physics* (Holt, New York, 1976).
[36] D. K. Schroder, *Semiconductor Material and Device Characterization*, 3rd ed. (John Wiley and Sons, Hoboken, 2006).
[37] B. Li, M. C. Tamargo, and C. A. Meriles, Appl. Phys. Lett. **91**, 222114 (2007).
[38] I. J. Lowe and D. Tse, Phys. Rev. **166**, 279 (1968).
[39] D. Y. Jeon, H. P. Gislason, J. F. Donegan, and G. D. Watkins, Phys. Rev. B **36**, 1324 (1987).

[40] D. Mao, P. C. Taylor, and W. D. Ohlsen, Phys. Rev. B **49**, 7952 (1994).

[41] I. Vurgaftman, J. R. Meyer, and L. Ram-Mohan, J. Appl. Phys. **89**, 5815 (2001).

[42] A. Goto, S. Kato, I. Turkevych, S. Ohki, T. Shimizu, K. Hashi, K. Takehana, T. Takamasu, and H. Kitazawa, J. Phys.: Conf. Ser. **150**, 022018 (2009).

[43] Y. P. Li, J. P. King, J. A. Reimer, and C. A. Meriles, Phys. Rev. B **88**, 235211 (2013).

[44] M. Engelsberg and R. E. Norberg, Phys. Rev. B **5**, 3395 (1972).

[45] F. X. Zach, J. Appl. Phys. **75**, 7894 (1994).

[46] E. F. Schubert, *Doping in III-V Semiconductors* (Cambridge University Press, New York, 1993).